THEORETICAL AND APPLIED MECHANICS
Article in Press (2026) DOI: https://doi.org/10.2298/TAM260123005C

FLOW PATTERNS AND BIFURCATIONS IN A Z-SHAPED CAVITY PART II: REFINEMENT OF CORNER AND EFFECT OF REYNOLDS NUMBER

Ebutalib Çelik and Ali Deliceoğlu

Abstract. This research builds upon Çelik's earlier study [1], which explored various flow patterns and constructed a bifurcation diagram for the flow with Stokes approximation in a Z-shaped domain driven by dual lids. In this study, enhanced solutions near the re-entrant corner are initially derived using the asymptotic matching technique. These solutions direct attention towards a comprehensive analysis of flow structures and behaviors at the re-entrant corner point. The formation and bifurcation of the separation bubble that appears near the corner is investigated in detail. Subsequently, the (h_1, h_2) control space diagram, which was previously developed on the basis of cavity height parameters, is recreated for a Reynolds number of 50. Additionally, the impact of the Reynolds number (Re) on vortex formation is analyzed. The findings indicate that at $Re = 50$, distinct flow patterns occur, and an increase in the Reynolds number accelerates vortex formation, leading to earlier transitions in flow topology and more complex bifurcation scenarios.

1. Introduction

Cavity flows, influenced by geometry, boundary conditions, and flow regimes, exhibit rich vortex structures and bifurcation phenomena that evolve as the Reynolds number increases. Cavity-type flows are significant in various engineering applications due to their complex dynamics and implications for performance and control [2–4]. Understanding these flows is essential for optimizing designs in aeronautics, heat transfer systems, and fluid mechanics, where accurate prediction of vortex behavior directly impacts efficiency and stability. Among the diverse cavity configurations studied in the literature, the Z-shaped cavity represents a distinctive geometry, offering unique challenges and opportunities for analyzing flow separation, vortex interaction, and bifurcation phenomena. Applied research has investigated flow structures in multi-bend and Z-shaped configurations [5–8]. Çelik [1] investigated flow patterns and vortex formation for incompressible, steady

2020 *Mathematics Subject Classification:* 76D05, 76M10, 65N50, 37N10.
Key words and phrases: Z-shaped, asymptotic solution, separation bubble, Reynolds effects.

flows with Stokes approximation in a Z-shaped cavity with two lids moving in the same direction, using numerical methods and nonlinear dynamical systems to analyze how flow structures change with varying cavity heights. He constructed a control-space diagram to map these transformations and detail the bifurcation scenarios that lead to the creation of new vortices. In subsequent research, Çelik et al. [9] also utilized the Z-shaped cavity geometry, but focused on the case where only the upper lid is in motion. By solving the flow analytically, paper specifically investigated the critical role of the separation line crossing the corner point in the genesis of new vortices. More recently, computational fluid dynamics analyses of Z-pipe geometries have highlighted the influence of circulating flows on separation efficiency and operational stability [10]. Complementary research has extended these insights to magnetohydrodynamic mixed convection in lid-driven Z-shaped cavities, revealing the interactions between Joule heating, rotating elements, and magnetic fields that produce intricate thermofluidic behavior [11].

In complex cavity geometries, singular points near corners often degrade numerical accuracy and stability. To overcome these challenges, several studies have developed specialized techniques [12]. Phillips [13] pioneered singular matched eigenfunction expansions for Stokes flow around corners, while Hawa and Rusak [14] extended asymptotic solutions through numerical-asymptotic expansion matching. More recent contributions, such as Deliceoğlu et al. [15], further refined eigenfunction-based treatments for viscous flows. Complementary approaches include combined analytical–numerical methods [16] and singularity-aware discretizations in modern computational frameworks. Additionally, studies on convective heat transfer enhancement [17] underscore the broader relevance of corner singularity treatment in thermofluid applications.

In fluid mechanics, the study of flow separation followed by reattachment, leading to separation bubbles, is crucial due to its impact on aerodynamic design and thermal efficiency. These bubbles cause performance losses in systems, including decreased lift, increased drag, and uneven surface heat transfer. The Laminar Separation Bubble (LSB), common in low Reynolds number applications, occurs when flow separates from the surface laminarly, transitions to turbulence within the recirculating area, and reattaches turbulently. The dynamics of separation bubbles and their impact on engineered systems have been extensively studied [18–23]. Some research efforts aim to better understand the formation, development, and transition of the separation bubble. Deliceoğlu and Aydin [24] investigated the complex interaction between the main internal flow (driven by the moving lid) and separation vortex formed at the sharp re-entrant corner of the L-shaped cavity. In recent studies, Xenos [25] focused on the mathematical modeling and preliminary numerical results for the LSB phenomenon in a compressible flow regime, aiming to build a theoretical framework. Kumar and Sarkar [26] investigated the Laminar Separation Bubble (LSB) under varying conditions using experiments and Large Eddy Simulation (LES).

Despite the extensive investigations into cavity-driven flows, the Z-shaped cavity continues to attract attention across engineering and applied sciences due to its distinctive geometry and the challenges posed by corner-induced singularities.

These singular points not only complicate numerical accuracy but also interact strongly with separation bubbles, which influence flow reattachment and vortex dynamics. Building on previous work [1], the present study advances this line of research by focusing on the corner regions through an asymptotic matching technique, enabling a more precise characterization of separation bubbles and their coupling with other flow structures. Furthermore, the previously established bifurcation diagram is extended at a constant Reynolds number ($Re = 50$), revealing new flow regimes and transitions. By solving the Navier–Stokes equations with a stabilized finite element method, this study provides a comprehensive framework for analyzing vortex formation, singularity effects, and bubble dynamics within the Z-shaped cavity, thereby contributing to the fundamental understanding of complex cavity-type flows.

2. Governing equations

The flow patterns identified by Çelik [1] will be analyzed locally near the corner using the matching technique. To achieve this, the polar form of the governing equations is derived for the Stokes flow approximation. Furthermore, the Navier–Stokes equations are formulated to explore the influence of the Reynolds number.

2.1. Separable solutions of the Stokes equations. The study of the local flow near the re-entrant corner is conducted using a polar coordinate system (r, θ). Consequently, we employ the separable solutions of the dimensionless Stokes equations for steady, planar flows. The stream function, which satisfies the biharmonic equation, is expressed in the polar form

$$\nabla^4\psi(r,\theta) = \Big(\frac{\partial^2}{\partial r^2} + \frac{1}{r}\frac{\partial}{\partial r} + \frac{1}{r^2}\frac{\partial^2}{\partial\theta^2}\Big)^2\psi(r,\theta) = 0,$$

where $u_r(r,\theta) = \frac{1}{r}\frac{\partial\psi}{\partial\theta}$ is the radial and $u_\theta(r,\theta) = -\frac{\partial\psi}{\partial r}$ is the circumferential velocity components, respectively. The solution of the steady flow around the corner of angle 2α formed by the wall $\theta = \mp\alpha$ takes the form by [27, 28],

$$\psi = \Re\Big\{\sum_{n=1}^{\infty}[A_n r^{\lambda_{a,n}} f_{\lambda_{a,n}}(\theta) + B_n r^{\lambda_{s,n}} f_{\lambda_{s,n}}(\theta)]\Big\}, \tag{2.1}$$

where

$$f_{\lambda_{a,n}}(\theta) = \cos((\lambda_{a,n}-2)\alpha)\cos(\lambda_{a,n}\theta) - \cos(\lambda_{a,n}\alpha)\cos((\lambda_{a,n}-2)\theta), \tag{2.2}$$

$$f_{\lambda_{s,n}}(\theta) = \sin((\lambda_{s,n}-2)\alpha)\sin(\lambda_{s,n}\theta) - \sin(\lambda_{s,n}\alpha)\sin((\lambda_{s,n}-2)\theta). \tag{2.3}$$

Unknown complex constants $A_n = a_n^r + ia_n^i$, $B_n = b_n^r + ib_n^i$ are determined by the least square sense. For a non-trivial solution, eigenvalues of (2.2)–(2.3), $\lambda_{a,n}$ and $\lambda_{s,n}$, satisfy equations

$$(\lambda_n - 1)\sin(2\alpha) + \sin(2\alpha(\lambda_n - 1)) = 0,$$
$$(\lambda_n - 1)\sin(2\alpha) - \sin(2\alpha(\lambda_n - 1)) = 0,$$

for anti-symmetric and symmetric flow, respectively.

2.2. Navier–Stokes equations. Governing equations in an open bounded domain $\Omega \subset I\!R^2$ with the boundary $\partial\Omega$ for the steady, viscous and incompressible flow are given in dimensionless form as follows:

$$\begin{cases} (\mathbf{u}\cdot\nabla)\mathbf{u} - \epsilon\Delta\mathbf{u} + \nabla p = \mathbf{f} & \text{in } \Omega, \\ \nabla\cdot\mathbf{u} = 0 & \text{in } \Omega, \\ \mathbf{u} = 0 & \text{on } \partial\Omega, \end{cases} \tag{2.4}$$

where $\mathbf{u}$ is velocity field, p and $\mathbf{f}$ are scalar pressure and a given source function, respectively. Reynolds number (Re) expresses the ratio of inertial forces to viscous forces. This system is derived from the conservation laws of momentum and mass in an incompressible fluid. The final condition enforces a no-slip boundary constraint, requiring the velocity field to vanish on the boundary $\partial\Omega$. The term $\mathbf{f}$ denotes a given body-force vector accounting for external forces acting on the fluid. For the numerical experiments reported in this paper, the source term is set to $\mathbf{f} = \mathbf{0}$. Due to the presence of nonlinear terms, the system is generally addressed through numerical techniques. In this study, the solutions of the equations are obtained numerically in a coupled form in terms of velocity components and pressure.

3. Numerical methods

3.1. Asymptotic matching method. In many cases, the current numerical methods applied to cavity problems fail to produce satisfactory outcomes at singular points near re-entrant or salient corners. To address this issue and enhance the accuracy of solutions at these singular points, various techniques have been devised (see, [13–15]). In our research, we employed the asymptotic matching method introduced by Deliceoğlu et al. [15] to refine the solutions around the corners. In this approach, numerical or analytical solutions at points sufficiently distant from the singularity are matched with the asymptotic solutions, thereby determining the behavior of the flow around the corner.

The detailed investigation of local flow characteristics is conducted using the asymptotic solution (2.1). As depicted in Figure 1, the current finite element method is employed to determine the flow properties at locations beyond the radius r_0 (first region). The numerical approach is matched with the asymptotic solution at points

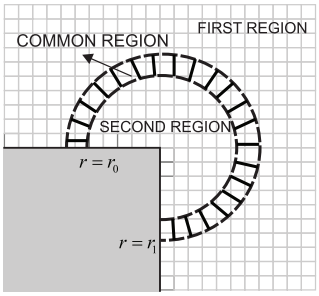

FIGURE 1. Display of points around the corner for the matching process.

within the $r_0 < r < r_1$ (common region), which are close to the corner yet distant from the singularity. The analysis of flow properties is carried out by considering solely the asymptotic solution when the radius is $r < r_0$ (second region).

In the first region, the stream function is derived using standard axes through the numerical method. Conversely, in the second region, where local trajectory analysis is conducted, a polar-type solution is sought using the asymptotic solution (2.1). The points lying in the common region are rewritten in polar form using the transformation $x = r\cos(\theta + \pi/4)$ and $y = r\sin(\theta + \pi/4)$ to facilitate the application of the matching method. Naturally, the velocity vector components obtained from both the numerical method and the asymptotic solution are equal at the points within the overlapping region. Therefore, the matching conditions are taken as $u_r^I = u_r^{II}$ and $u_\theta^I = u_\theta^{II}$, where the superscripts indicate the region to which the vector components belong. Initially, the anti-symmetric term of the asymptotic solution (2.1) is considered during the matching process. Therefore, the first N terms for anti-symmetric flow are used to approximate the stream function solution. By applying the least-squares method to the points within the matching zone, the total squared error across all points is determined as follows:

$$E^2 = \sum_{k=1}^{M} \left\{ -u_r^{II}(r_k,\theta_k) + \sum_{j=1}^{N}(a_j^r\phi_j(\theta_k) - a_j^i\mu_j(\theta_k)) \right\}^2 + \sum_{k=1}^{M} \left\{ -u_\theta^{II}(r_k,\theta_k) + \sum_{j=1}^{N}(a_j^r\varphi_j(\theta_k) - a_j^i\omega_j(\theta_k)) \right\}^2,$$

where

$$\phi_j = \Re[f'_{aj}(\theta)r^{\lambda_{aj}-1}], \qquad \mu_j = \Im[f'_{aj}(\theta)r^{\lambda_{aj}-1}],$$
$$\varphi_j = \Re[-\lambda_{aj}f_{aj}(\theta)r^{\lambda_{aj}-1}], \quad \omega_j = \Im[-\lambda_{aj}f_{aj}(\theta)r^{\lambda_{aj}-1}],$$

and the coordinates $(r_1,\theta_1),\ldots,(r_M,\theta_M)$ represent the locations of points surrounding the re-entrant corner. The function E^2 serves as an error function for the constant variables a_j^r, a_j^i. By differentiating this error function with respect to a_j^r, a_j^i to minimize it, a linear equation system $Ax = B$ is formed, containing $2N$ unknown real scalars $\{a_j, b_j, j = 1,\ldots,N\}$. This system can be resolved for the unknowns using the standard Gauss elimination method implemented in FORTRAN on a computer, allowing for a detailed examination of local flow properties (refer to [15] for more information).

3.2. Finite element formulation for Navier–Stokes equations. In this research, the coupled system (2.4) is numerically solved using the finite element method. Stabilized finite element methods involve incorporating mesh-dependent terms into the standard Galerkin finite element formulation to stabilize the system. There are many studies with stabilized finite element methods for incompressible Navier–Stokes equations [29–31], and analysis can be found in [32]. The weak formulation of problem (2.4) can be expressed utilizing the two function spaces $V = (H_0^1(\Omega))^2$ and $P = C^0(\bar{\Omega}) \cap L_0^2(\Omega)$ [33]: Find $\mathbf{u} \in V$, $p \in P$ such that for all

$\mathbf{v} \in V,\ q \in P$

$$B(\mathbf{u};\mathbf{u},p;\mathbf{v},q) = (\mathbf{f},\mathbf{v}), \tag{3.1}$$

where $B(\mathbf{u};\mathbf{u},p;\mathbf{v},q)$ is as $(\nabla\mathbf{u})\mathbf{u},\mathbf{v}+\epsilon(\nabla\mathbf{u},\nabla\mathbf{v})-(\nabla\cdot\mathbf{v},p)+(\nabla\cdot\mathbf{u},q)$ and $\epsilon = 1/\mathrm{Re}$. The mixed finite element approximation of problem (3.1) is established through the selection of finite-dimensional subspaces $V_h \subset V$ and $P_1 \subset P$, which are defined on a series of discretizations T_h of the domain Ω.

It is well-established that the decomposition of a domain into regular geometric elements, such as rectangles or triangles, does not yield stable results within a standard Galerkin finite element framework. As mentioned above, we employ the stabilizing sub-grid method to achieve more stable solutions. We assume that T_h consists of regular triangles $\{K\}$. Furthermore, we define the following finite-dimensional subspaces on T_h:

$$V_h = V_1 \oplus \bigcup_{K\in T_h} (B(K))^2 = \{\mathbf{v} \in (\mathbf{H_0^1(\Omega)})^\mathbf{2} | \mathbf{v}|_\mathbf{K} \in (\mathbf{P_1(K)} \oplus \mathbf{B(K)})^\mathbf{2},\ \mathbf{K} \in \mathbf{T_h}\},$$

where

$$V_1 = \{\mathbf{v} \in (H_0^1(\Omega))^2\, |\mathbf{v}|_\mathbf{K} \in \mathbf{P_1(K)^2},\ \mathbf{K} \in \mathbf{T_h}\},$$
$$P_1 = \{p \in C^0(\bar{\Omega}) \cap L_0^2(\Omega)\, |p|_K \in P_1(K),\ K \in T_h\},$$

$B(K)$ is the space of the residual-free bubble functions which are defined in [34].

Then, the Galerkin finite element formulation of the problem is written as follows: find the pair $\{\mathbf{u}_h = \mathbf{u}_1 + \mathbf{u}_b, p_1\}$ from $V_h \times P_1$ such that $\forall\{\mathbf{v}_h, q_1\} \in V_h \times P_1$ where

$$B(\mathbf{u}_h;\mathbf{u}_h,p_1;\mathbf{v}_h,q_1) = (\mathbf{f},\mathbf{v}_h) = ((\nabla\mathbf{u}_h)\mathbf{u}_h,\mathbf{v}_h) + \epsilon(\nabla\mathbf{u}_h,\nabla\mathbf{v}_h) - (\nabla\cdot\mathbf{v}_h,p_1) + (\nabla\cdot\mathbf{u}_h,q_1). \tag{3.2}$$

The problem (3.2) is non-linear due to the inclusion of the advection term. An iterative process is used to overcome this difficulty such that we decompose the approximate solutions $\mathbf{u}_h$ and p_1 as $\mathbf{u}_h^{n+1} = \mathbf{u}_h^n + \hat{\mathbf{u}}_h,\ p_1^{n+1} = p_1^n + \hat{p}_1$ where the variables $\mathbf{u}_h^{n+1}$ and p_1^{n+1} represent the approximations at the current iteration step, while $\mathbf{u}_h^n$ and p_1^n denote the approximations at the preceding iteration step. The terms $\hat{\mathbf{u}}_h$ and $\hat{p}_1$ correspond to the corrections applied to the approximations from the previous iteration step.

The stabilized finite element formulation of the problem can be written as follows by employing this linearisation and appending the bubble function values [35]: Find $\{\mathbf{u}_1^{n+1}, p_1^{n+1}\} \in V_1 \times P_1$ such that $\forall\{\mathbf{v}_1, q_1\} \in V_1 \times P_1$

$$B(\mathbf{u}_1^n;\mathbf{u}_1^{n+1},p_1^{n+1};\mathbf{v}_1,q_1) + \sum_{K\in T_h} \tau_K \int_K [(\nabla\mathbf{u}_1^{n+1})\mathbf{u}_1^n + \nabla p_1^{n+1} - \mathbf{f}][(\nabla\mathbf{v}_1)\mathbf{u}_1^n - \nabla q_1] = (\mathbf{f},\mathbf{v}_1),$$

where

$$B(\mathbf{u}_1^n;\mathbf{u}_h^{n+1},p_1^{n+1};\mathbf{v}_1,q_1) = ((\nabla\mathbf{u}_h^{n+1})\mathbf{u}_1^n,\mathbf{v}_1) + \epsilon(\nabla\mathbf{u}_h^{n+1},\nabla\mathbf{v}_1) - (\nabla\cdot\mathbf{v}_1,p_1^{n+1}) + (\nabla\cdot\mathbf{u}_h^{n+1},q_1),$$

and the stabilization parameter τ_K is calculated approximately as given in [36]. See [36, 37] for detailed information on the stabilization process.

4. Qualitative analysis of streamlines

This section presents a qualitative analysis of the streamlines to understand the structure of the flow patterns, particularly near the corner within the cavity, and the transition of this structure. In this analysis, the term "flow bifurcation" refers to a change in the nature of the critical point. Generally, there are two types of critical points: in-flow and no-slip. In-flow critical points have zero flow velocity, whereas no-slip critical points have zero vorticity. Consider an incompressible 2D flow. There is a stream function ψ such that $\dot{x} = u = \frac{\partial \psi}{\partial y}$, $\dot{y} = v = -\frac{\partial \psi}{\partial x}$.

To analyze the structure of in-flow critical points locally, the velocity field is expanded in a Taylor series as:

$$\psi = \sum_{i+j=1}^{\infty} a_{ij} x^i y^j \tag{4.1}$$

whose coefficients have a direct physical interpretation. First order coeefficients are related to velocity field, so the linear approximation of streamlines (4.1) is

$$\begin{pmatrix} \dot{x} \\ \dot{y} \end{pmatrix} = \begin{pmatrix} a_{01} \\ -a_{10} \end{pmatrix} + \begin{pmatrix} a_{11} & 2a_{02} \\ -2a_{10} & -a_{11} \end{pmatrix} \begin{pmatrix} x \\ y \end{pmatrix}. \tag{4.2}$$

If we assume that the critical points are the origin, then $a_{01} = a_{10} = 0$. Based on Hamiltonian systems theory, the determinant of the Jacobian matrix of (4.2) determines the structure of the flow: if $|J| > 0$, the critical point is a center; if $|J| < 0$, it is a saddle point, Figure 2a. For more details about in-flow critical points, see [38]. Hartnack [39] presented the stream function at no-slip critical points in the form of a power series as $\psi = y^2 \sum_{i+j=0}^{\infty} a_{ij} x^i y^j$, which has y^2 factor because of the boundary condition on the wall. In a similar way, (4.2) is reduced

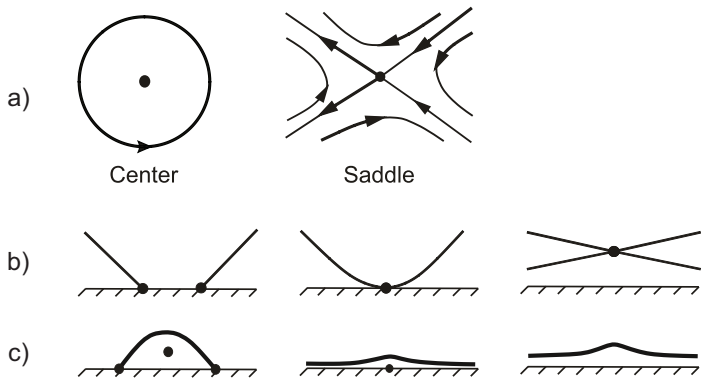

FIGURE 2. Streamline patterns a) at in-flow b) near a stationary wall for $\sigma = -1$ c) near a stationary wall for $\sigma = 1$

to the dynamical system with the Jacobian

$$J = \begin{pmatrix} 2a_{12} & 3a_{03} \\ 0 & -a_{12} \end{pmatrix}.$$

Under non-degenerate condition ($a_{12} \neq 0$), the critical point is a hyperbolic saddle, which is either a point of separation or attachment depending on the sign of coefficient a_{12} related to wall shear stress. He used the normal form transformation to determine the local streamline pattern for higher-order terms when ($a_{12} = 0$). Then, he presented the normal form of the stream function at fourth order as $\psi = y^2(\sigma y + c_0 + 0.5x^2)$. He constructed a bifurcation diagram depending on σ and c_0 that shows the formation of a separation bubble and the merging of two separation bubbles, as shown in Figure 2b and Figure 2c. For a higher-order normal form and the transformation of the streamline, see [39].

5. Numerical results

The boundary value problem formed for steady, viscous and incompressible flow in the two-dimensional Z-shaped cavity, as shown in Figure 3, was solved numerically for $Re = 0$ [1]. By altering the cavity heights h_1 and h_2, Çelik [1] identified various flow patterns within the Z-shaped domain and constructed a control space diagram for the ranges $-1.8 < h_1 < -1.4$ and $1.4 < h_2 < 1.8$, which includes both salient and re-entrant corners. The bifurcation diagram is illustrated again in Figure 4.

The diagram features several bifurcation lines that depict different types of bifurcations. Bifurcation refers to the change in the nature of a critical point. Near a stationary wall, a bifurcation occurs where two saddle points on the wall merge to form a saddle point off the wall. This type of bifurcation is represented by $BM_i, (i = 1, 2)$. Besides the points on the wall, there are off-wall points that split into a saddle and a center, illustrating a cusp bifurcation, with the corresponding curves marked as $CP_i, (i = 1, \ldots, 5)$. The creation of a bubble on the stationary

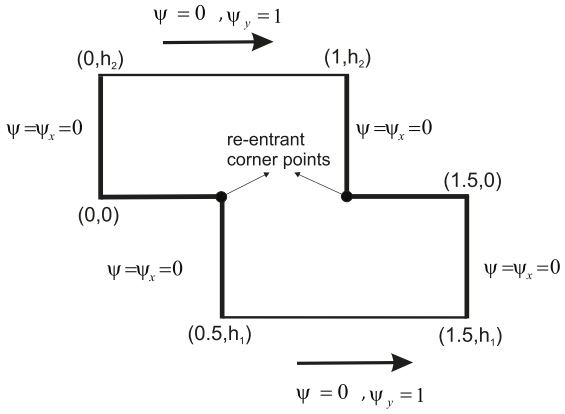

FIGURE 3. Boundary conditions for the lid-driven Z-shaped cavity.

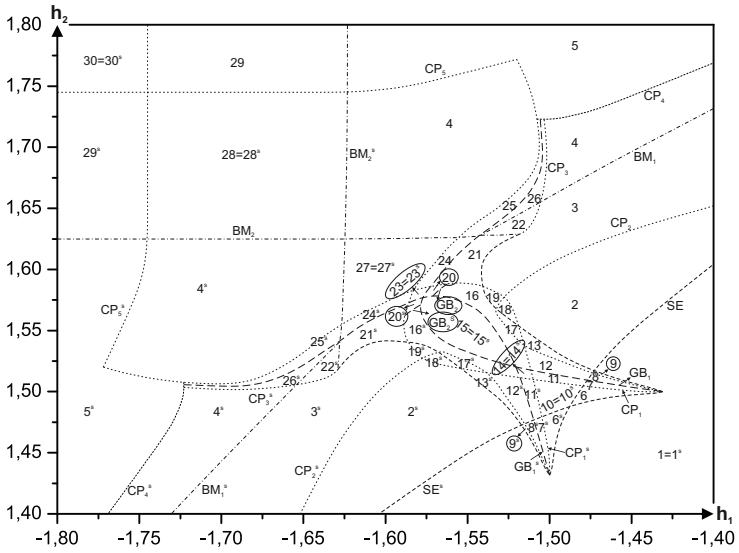

FIGURE 4. Bifurcation diagram for the double lid-driven Z-shaped cavity generated by Çelik [1].

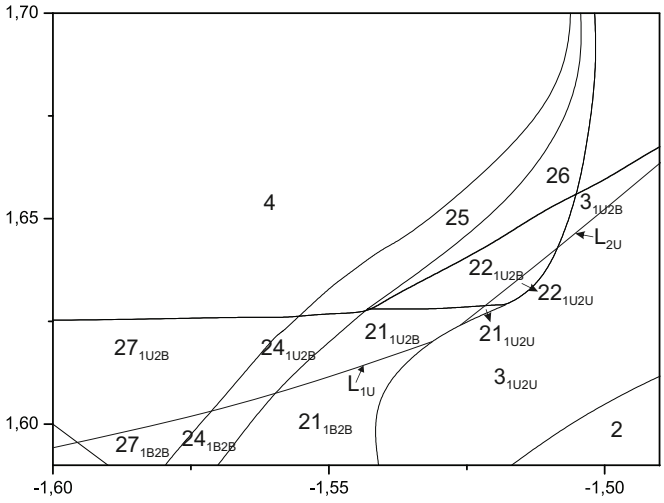

FIGURE 5. Enlarged view of the control space diagram region (Figure 4) where the separation bubble is formed.

wall is indicated by SE. The stream function value at the interior saddle point can match the values of the critical points on the walls, leading to a global bifurcation curve, denoted as $GB_i, (i = 1, 2)$. For detailed information on bifurcation of critical points, see [38–40].

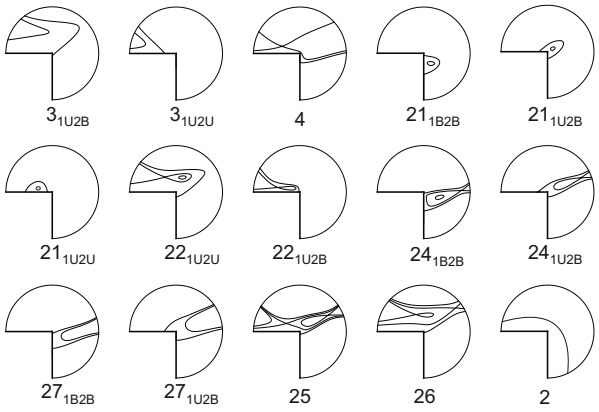

FIGURE 6. Detailed examination of the flow structures around the corner point using the matching method.

5.1. Detailed examination of flow patterns around the re-entrant corner. Among the intriguing subjects in the study of low-numbered Reynolds flows is the separation bubble that forms within the flow. Investigating the structural bifurcations of the separation bubble and its role in the eddy mechanism is challenging due to its small size and its tendency to appear primarily at corner points in cavity flow problems. Consequently, this section aims to enhance existing numerical solutions by employing the asymptotic matching method. It will thoroughly examine the structural transformations of the separation bubble at the re-entrant corner point, influenced by variations in the control space parameters (h_1, h_2). Additionally, the impact of these transformations on the curves in the previously derived control space diagram and the regions defined by these curves will be explored.

The section of the control space diagram where the separation bubble forms is once again determined using the asymptotic matching method and is expanded as illustrated in Figure 5. Corresponding flow patterns of the regions in Figure 5 are plotted in Figure 6.

Tracking the flow patterns and their bifurcations is relatively straightforward by following any path in Figure 5. However, it is important to highlight the phase of the separation bubble. As indicated in (21_{1B2B}) in Figure 6, the two branches of the separation bubble are positioned below the corner point and along the vertical sidewall. When crossing the curve L_{1u} from region (21_{1B2B}) to (21_{1U2B}), the separation bubble ascends along the sidewall, and the branch reaches the re-entrant corner, then transitions to the horizontal wall by crossing the corner point (refer to (21_{1U2B}) in Figure 6). As we proceed from region (21_{1U2B}) to (21_{1U2U}) by crossing the curve L_{2u}, the second branch of the separation bubble moves through the corner point toward the horizontal wall, and the separation bubble is now entirely on the horizontal wall (see (21_{1U2U}) in Figure 6). Figure 7 illustrates the interaction between the separation bubble formed near the corner point and other internal flow structures.

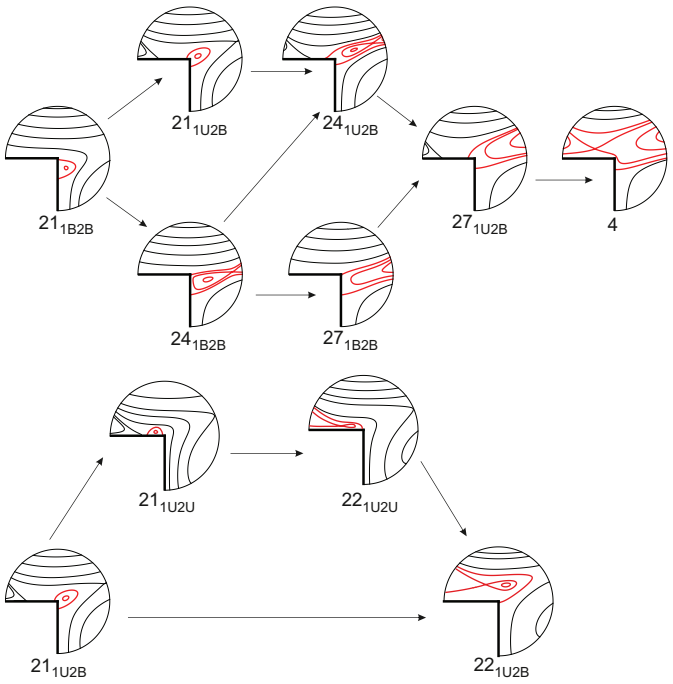

FIGURE 7. Bifurcations occurring around the corner point and their interactions.

6. Regained control space diagram for $Re = 50$

In this section, the flow bifurcations within the Z-shaped cavity, as described by the Navier–Stokes equation, are examined using the previously mentioned stabilized finite element method. By varying h_1 and h_2 while keeping the Reynolds number constant, we derive the flow patterns and their bifurcation curves. The control space diagram is constructed for the interval $-1.8 \leqslant h_1 \leqslant -1.4$ and $1.4 \leqslant h_2 \leqslant 1.8$, similar to the previous study. The Reynolds number is set at $Re = 50$, and its influence on the bifurcation diagram is analyzed. The transition from two to four eddies in the cavity takes place within a small region of the control space diagram. This allows us to identify and depict all bifurcation curves within this confined area of the control space diagram for this specific Reynolds number. Figure 8 displays numerous bifurcation curves and regions, most of which are identical to those found at $Re = 0$. These identical curves result in the formation of topologically similar flow patterns in the regions, which are labeled with the same names as the corresponding regions in Figure 4. Figure 9 illustrates the flow patterns for region 28 at $Re = 0$ and $Re = 50$. The flow patterns are topologically identical in both cases.

However, for $Re = 0$, the region is defined by $-1.77 \leqslant h_1 \leqslant -1.64$ and $1.74 \leqslant h_2 \leqslant 1.725$, whereas for $Re = 50$, it is defined by $-1.75 \leqslant h_1 \leqslant -1.575$ and $1.6 \leqslant h_2 \leqslant 1.69$. Comparing the bifurcation curves for region 28 reveals that

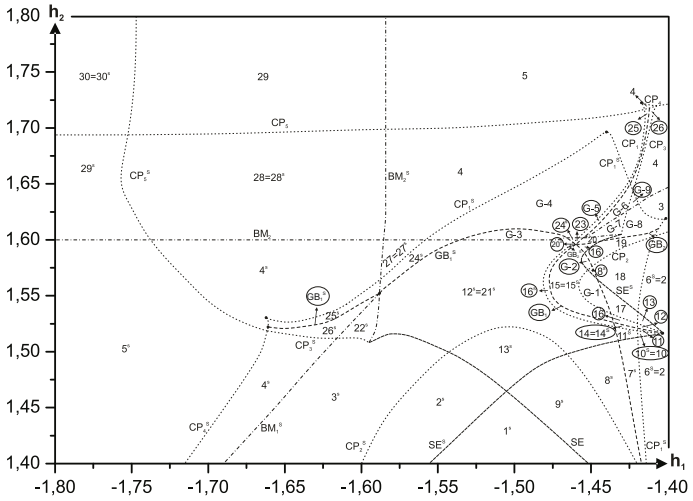

FIGURE 8. Control-space diagram for $Re = 50$. The labels in each region are related to the flow patterns in Figure 4.

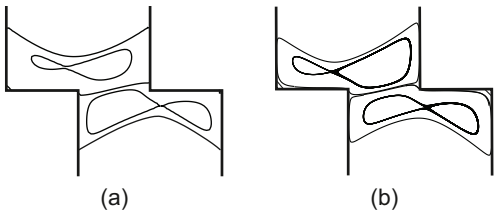

FIGURE 9. Streamlines for the region 28 for a) $Re = 0$, b) $Re = 50$

this region emerges at earlier values of h_1 and h_2 for $Re = 50$. In the ongoing comparison between Figure 8 (for $Re = 50$) and Figure 4 (for $Re = 0$), a significant transformation in the shape of the bifurcation curves is observed. Notably, in Figure 8, the curves lose their symmetry with respect to the line $y = -x$. Additionally, the curves for $Re = 50$ shift to the right in the control space diagram and become

TABLE 1. h_1 and h_2 values in which the second vortex in the upper cavity is formed.

h_1	$Re = 0$	$Re = 50$	$Re = 100$	$Re = 1000$
-1.40	$h_2 = 1.769$	$h_2 = 1.723$	$h_2 = 1.558$	$h_2 = 1.275$
-1.50	$h_2 = 1.723$	$h_2 = 1.695$	$h_2 = 1.553$	$h_2 = 1.277$
-1.60	$h_2 = 1.751$	$h_2 = 1.687$	$h_2 = 1.552$	$h_2 = 1.277$
-1.70	$h_2 = 1.742$	$h_2 = 1.684$	$h_2 = 1.551$	$h_2 = 1.278$
-1.80	$h_2 = 1.740$	$h_2 = 1.683$	$h_2 = 1.551$	$h_2 = 1.278$

intertwined. Consequently, some regions disappear (such as 20-21-22-23-24 in Figure 4), while new regions emerge. New flow patterns in these regions are illustrated in Figure 10.

Table 1 presents the h_1 and h_2 values for the formation of the second eddy generation in the upper section of the cavity. When h_1 is held constant, it is observed that h_2 values decrease as Re increases from 0 to 1000. The impact of the Reynolds number is that the vortex formation mechanism initiates at lower (h_1, h_2) values.

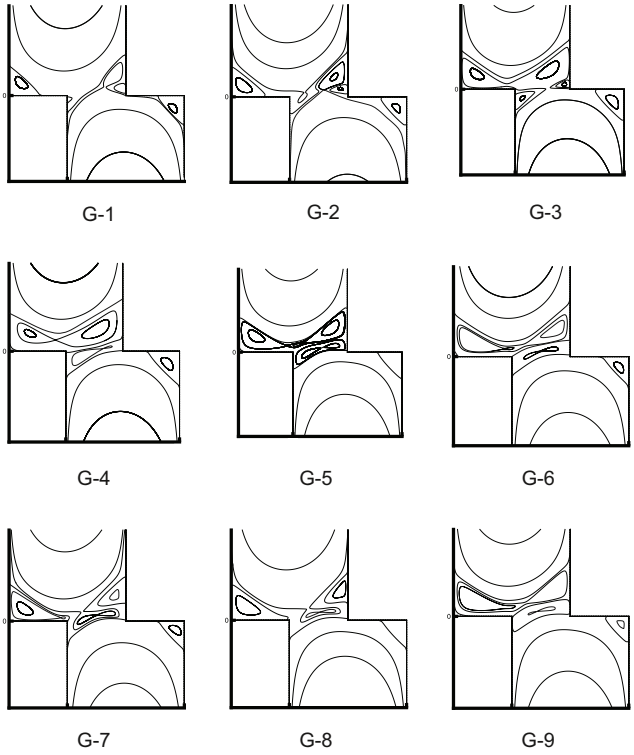

FIGURE 10. Streamline patterns for $Re = 50$ which cannot be observed for $Re = 0$.

7. Conclusion

In this study, flow patterns and bifurcation mechanisms in a lid-driven Z-shaped cavity have been investigated with particular emphasis on the refinement of corner solutions and the influence of the Reynolds number. Building upon the earlier Stokes flow analysis of Çelik [1], the present study extends the investigation by incorporating asymptotic matching techniques to improve the resolution of flow structures near the re-entrant corner and by examining inertial effects through the Navier–Stokes equations.

The detailed structure of the separation bubble forming near the corner has been clarified by matching the numerical solution with local asymptotic expansions. The evolution of this separation bubble, including its migration across the corner and its interaction with the cavity walls, has been systematically analyzed within the control space defined by the geometric parameters (h_1, h_2). The refined analysis reveals that the corner region plays a critical role in triggering local and global bifurcations that govern the overall flow topology.

Furthermore, the control-space diagram previously constructed under the Stokes approximation has been successfully regenerated for a finite Reynolds number of $Re = 50$. Although many bifurcation curves and flow patterns remain topologically similar to the creeping-flow case, the inclusion of inertial effects leads to significant quantitative and qualitative changes. In particular, the symmetry of the bifurcation diagram is lost, bifurcation curves shift and intersect, and several regions observed at $Re = 0$ disappear while new flow regimes emerge. These results demonstrate that even moderate Reynolds numbers can substantially alter the bifurcation structure.

The parametric study on the Reynolds number further indicates that increasing Re promotes earlier generation of secondary vortices in the cavity. For fixed geometric parameters, the critical values of h_2 at which new eddies appear decrease monotonically as the Reynolds number increases. This finding highlights the strong coupling between inertial effects and geometric confinement in determining flow transitions and vortex dynamics in complex cavity flows.

Despite these contributions, the present study has certain limitations. The analysis is restricted to two-dimensional, steady, incompressible flows, and unsteady effects or three-dimensional instabilities, which may become important at higher Reynolds numbers, are not considered. In addition, the asymptotic matching procedure is applied only in the vicinity of a single re-entrant corner and is based on Stokes-type local solutions, which may become undetermined at higher Reynolds numbers. Future work may address these limitations by extending the analysis to unsteady and three-dimensional flows, exploring higher Reynolds numbers, and incorporating adaptive numerical techniques to further improve resolution near singular points.

Acknowledgments. The authors are supported by the Scientific and Technological Research Council of Türkiye under Grant No. 114F525.

References

1. E. Çelik, *Flow patterns and bifurcations in a Z-shaped cavity*, Erciyes Üniv. Fen Bilim. Enst. Fen Bilim. Derg. **36**(3) (2020), 408–419.
2. J. Lin, *Finite element modeling of heat transfer in Z-shaped cavity according to constructal design*, Proc. Indian Natl. Sci. Acad. **89** (2023), 967–976.
3. A. M. Aly, S.-W. Lee, N. Alsedais, *The magnetic field on the bioconvection flow of NEPCM in a Z-shaped cavity containing three circular cylinders*, Chin. J. Phys. **92** (2024), 253–269.
4. M. N. A. Omi, M. A. Khan, *Discretization of thermofluidic behavior of the combined effects of MHD conjugate mixed convection and joule heating in a lid-driven Z-shaped cavity containing double rotating cylinders*, Heat Transf. **55**(1) (2026), 448–468.

5. J. Y. Tang, J. M. Chen, H. B. Ma, et al., *Numerical analysis of flow field characteristics in three-Z-shaped ultrasonic flowmeter*, Appl. Mech. Mater. **226–228** (2012), 1829–1834.
6. A. Ziganshin, E. Solodova, K. Logachev, *Numerical simulation of a Z-shaped ventilation elbow and reduction of its resistance*, IOP Conf. Ser., Mater. Sci. Eng. **890** (2020), 012146.
7. C. Zhou, J. Su, X. Jiang, Z. Shi, *Numerical simulation and experimental verification for the sorting behaviors of mixed biomass particles in a novel Z-shaped fluidized bed*, Chem. Eng. J. **441** (2022), 136109.
8. K. Zhao, C. Song, W. Pan, Y. Li, Y. Yan, Y. Lei, *Flow resistance and synergy analysis in Z-shaped combined bend*, J. Build. Eng. **105** (2025), 112482.
9. E. Çelik, M. Luzum, A. Deliceoğlu, *Stokes flow in a Z-shaped cavity with moving upper lid*, Karaelmas Fen ve Müh. Derg. **11**(1) (2021), 12–22.
10. Y. Dai, X. Ma, B. Li, H. Xu, J. Kui, M. Qiu, B. Liang, G. Wen, X. Song, *Flow field analysis of Z-pipe based on circulating flow CFD method*, In: Y. Wang, T. Yu, K. Wang (eds), *Advanced Manufacturing and Automation XIV, IWAMA 2024*, Lecture Notes in Electrical Engineering **1364**, 576–588, Springer, Singapore, 2025.
11. M. N. A. Omi, M. A. Khan, *Discretization of thermofluidic behavior of the combined effects of MHD conjugate mixed convection and joule heating in a lid-driven Z-shaped cavity containing double rotating cylinders*, Heat Transf. **55** (2025), 448–468.
12. D. N. Pham, S. Bharadwaj, S. Rodriguez, L. Rodriguez, L. R. Ram-Mohan, *High-accuracy calculation of singular electromagnetic fields in regions with re-entrant peripheries*, J. Appl. Phys. **134**(15) (2023), 153102.
13. T. Phillips, *Singular matched eigenfunction expansions for Stokes flow around a corner*, IMA J. Appl. Math. **42**(1) (1989), 13–26.
14. T. Hawa, R. Rusak, *Numerical-asymptotic expansion matching for computing a viscous flow around a sharp expansion corner*, Theor. Comput. Fluid Dyn. **15**(5) (2002), 265–281.
15. A. Deliceoğlu, E. Çelik, F. Gürcan, *Singular treatment of viscous flow near the corner by using matched eigenfunctions*, Proc. IMechE, Part C: J. Mech. Eng. Sci. **233**(5) (2019), 1660–1676.
16. J. M. Shi, M. Breuer, F. Durst, *A combined analytical-numerical method for treating corner singularities in viscous flow predictions*, Int. J. Numer. Methods Fluids **45** (2004), 659–688.
17. Y. Menni, A. Azzi, A. Chamkha, *Enhancement of convective heat transfer in smooth air channels with wall-mounted obstacles in the flow path: A review*, J. Therm. Anal. Calorimetry 135(4) (2019), 1951–1976.
18. W. B. Roberts, *Calculation of laminar separation bubbles and their effect on airfoil performance*, AIAA J. **18** (1980), 25–31.
19. Y. K. Shum, D. J. Marsden, *Separation bubble model for low Reynolds number airfoil applications*, J. Aircraft **31** (1994), 761–766.
20. A. Hatman, T. Wang, *Separated-flow transition: Part 3 — primary modes and vortex dynamics*, In: *Proceedings of the ASME 1998 International Gas Turbine and Aeroengine Congress and Exhibition, Volume 1: Turbomachinery*, V001T01A109, June 2–5, 1998, Stockholm, Sweden, ASME, 1998.
21. A. Choudhry, M. Arjomandi, R. Kelso, *A study of long separation bubble on thick airfoils and its consequent effects*, Int. J. Heat Fluid Flow **52** (2015), 84–96.
22. H. Dong, T. Xia, L. Chen, S. Liu, Y. D. Cui, B. C. Khoo, A. Zhao, *Study on flow separation and transition of the airfoil in low Reynolds number*, Phys. Fluids **31**(10) (2019), 103601.
23. J. A. Smith, G. Pisetta, I. M. Viola, *The scales of the leading-edge separation bubble*, Phys. Fluids **33** (2021).
24. A. Deliceoğlu, S. H. Aydin, *Flow bifurcation and eddy genesis in an L-shaped cavity*, Comput. Fluids **73** (2013), 24–46.
25. M. A. Xenos, *Mathematical formulation of bubble formation after compressible boundary layer separation: Preliminary numerical results*, Open J. Fluid Dyn. **12** (2022), 304–320.
26. R. Kumar, S. Sarkar, *Features of laminar separation bubble subjected to varying adverse pressure gradients*, Phys. Fluids **35**(12) (2023), 124104.

27. H. Moffatt, *Viscous and resistive eddies near a sharp corner*, J. Fluid Mech. **18**(1) (1964), 1–18.
28. P. Shankar, *Slow Viscous Flows: Qualitative Features and Quantitative Analysis Using Complex Eigenfunction Expansions*, Imperial College Press, London, 2007.
29. L. P. Franca, S. L. Frey, *Stabilized finite element methods: II. the incompressible Navier–Stokes equations*, Comput. Methods Appl. Mech. Eng. **99**(2-3) (1992), 209–233.
30. L. P. Franca, A. I. Nesliturk, *On a two-level finite element method for the incompressible Navier–Stokes equations*, Int. J. Numer. Methods Eng. **52**(4) (2001), 433–453.
31. J. F. Gerbeau, *A stabilized finite element method for the incompressible magnethydrodynamic equations*, Numer. Math. **87** (2000), 83–111.
32. H. G. Roos, M. Stynes, L. Tobiska, *Numerical Methods for Singularly Perturbed Differential Equations*, Springer Berlin, Heidelberg, 1996.
33. E. Becker, G. Carey, J. Oden, *Finite Elements, An Introduction*, Vol. I, Prentice-Hall, New Jersey, 1981.
34. P. Ciarlet, *The Finite Element Methods for Elliptic Problems*, North-Holland, Amsterdam, 1978.
35. A. Russo, *Bubble stabilization of finite element methods for the linearized incompressible Navier–Stokes equations*, Comput. Methods Appl. Mech. Eng. **132** (1996), 335–343.
36. A. Nesliturk, S. Aydın, M. Tezer-Sezgin, *Two-level finite element method with a stabilizing subgrid for the incompressible Navier–Stokes equations*, Int. J. Numer. Methods Fluids **58** (2008), 551–572.
37. F. Brezzi, D. Marini, A. Russo, *On the choice of a stabilizing subgrid for convection–diffusion problems*, Comput. Methods Appl. Mech. Eng. **194** (2005), 127–148.
38. M. Brøns, J. Hartnack, *Streamline topologies near simple degenerate critical points in two-dimensional flow away from boundaries*, Phys. Fluids **11**(2) (1999), 314–324.
39. J.Hartnack, *Streamline topologies near a fixed wall using normal forms*, Acta Mech. **136**(1) (1999), 55–75.
40. F. Gurcan, A. Deliceoğlu, P. Bakker, *Streamline topologies near a non-simple degenerate critical point close to a stationary wall using normal forms*, J. Fluid Mech. **539** (2005), 299–311.

ОБРАСЦИ ТОКА И БИФУРКАЦИЈЕ У ШУПЉИНИ Z-ОБЛИКА ДРУГИ ДЕО: ПРЕЦИЗИРАЊЕ УГЛА И ЕФЕКАТ РЕЈНОЛДСОВОГ БРОЈА

Резиме. Ово истраживање се надовезује на Челиков чланак [1], у коме су истражени различити обрасци тока и у коме је конструисан дијаграм бифуркације за ток са Стоксовом апроксимацијом у домену облика Z вођен дуалним поклопцима. У овој раду, су побољшана решења близу повратног угла, првобитно изведена коришћењем технике асимптотског подударања. Ова решења усмеравају пажњу на свеобухватну анализу структура и понашања тока у тачки повратног угла. Детаљно се истражује формирање и бифуркација мехура раздвајања који се појављује близу граничног угла. Након тога, дијаграм контролног простора $(h1, h2)$, који је претходно развијен на основу параметара висине шупљине, рекреиран је за вредност Рејнолдсовог броја 50. Поред тога, анализиран је утицај Рејнолдсовог броја (Re) на формирање вртлога. Резултати показују да се при $Re = 50$ јављају различити обрасци протока, а повећање Рејнолдсовог броја убрзава формирање вртлога, што доводи до ранијих прелаза у топологији протока и сложенијих сценарија бифуркације.

Department of Computer Technologies
Çanakkale Onsekiz Mart University
Çanakkale
Turkey
e.celik@comu.edu.tr
https://orcid.org/0000-0002-4500-4465

Department of Mathematics
Erciyes University
Kayseri
Turkey
adelice@erciyes.edu.tr
https://orcid.org/0000-0003-0863-6276

(Received 23.01.2026)
(Revised 31.03.2026)
(Available online 05.06.2026)